


Temperature distributions and gradients in laser-heated plasmas relevant to magnetized liner inertial fusion

K. R. Carpenter¹* and R. C. Mancini*Physics Department, University of Nevada, Reno, Nevada 89557, USA*

E. C. Harding, A. J. Harvey-Thompson, M. Geissel, M. R. Weis, S. B. Hansen, K. J. Peterson, and G. A. Rochau

Sandia National Laboratories, P.O. Box 5800, Albuquerque, New Mexico 87185, USA (Received 27 May 2020; accepted 28 July 2020; published 24 August 2020)

We present two-dimensional temperature measurements of magnetized and unmagnetized plasma experiments performed at Z relevant to the preheat stage in magnetized liner inertial fusion. The deuterium gas fill was doped with a trace amount of argon for spectroscopy purposes, and time-integrated spatially resolved spectra and narrow-band images were collected in both experiments. The spectrum and image data were included in two separate multiobjective analysis methods to extract the electron temperature spatial distribution $T_e(r, z)$. The results indicate that the magnetic field increases T_e , the axial extent of the laser heating, and the magnitude of the radial temperature gradients. Comparisons with simulations reveal that the simulations overpredict the extent of the laser heating and underpredict the temperature. Temperature gradient scale lengths extracted from the measurements also permit an assessment of the importance of nonlocal heat transport.

DOI: [10.1103/PhysRevE.102.023209](https://doi.org/10.1103/PhysRevE.102.023209)

I. INTRODUCTION

Magnetized liner inertial fusion (MagLIF) [1] is a pulsed-power-driven inertial confinement fusion (ICF) concept that has proven capable of producing thermonuclear conditions [2,3]. In MagLIF, fusion fuel is heated and compressed by a surrounding Be liner that has been imploded on axis by the $\mathbf{J} \times \mathbf{B}$ force created when current from the Z-Machine at Sandia National Laboratories (SNL) is applied to the liner's surface. Prior to implosion, the fuel is magnetized with a ~ 10 T external axial magnetic field and heated with a multikilojoule, multianosecond laser pulse from the Z-Beamlet laser (ZBL) [4]. The combination of the thermal conduction limiting magnetic field and laser-preheat reduces the convergence required to reach thermonuclear conditions [1,2].

Magneto-hydrodynamics (MHD) simulations have played an integral part in the development of MagLIF. They have been used to design experiments [5], explore ways to improve performance [6], and predict how MagLIF would scale on larger pulsed-power drivers [7]. The most complete simulations model the entire experiment, including the laser heating of both the fuel and the polyimide foil that covers the laser entrance hole (LEH) at the top of the liner [5]. These simulations have indicated that the conditions at stagnation are dependent on the amount of laser energy deposited into the fuel and that the optimal amount of coupled energy is determined by the fuel density, current drive, and axial magnetic field strength [1,7]. Due to the strong influence of the preheat stage on MagLIF performance, experiments dedicated to understanding the relevant physics are needed to ensure that accurate models are used to simulate the laser heating.

Laser-heating studies relevant to MagLIF have been performed on OMEGA at the Laboratory for Laser Energetics in Rochester, New York, USA [8,9], where the time evolution of the spatially averaged electron temperature [8] and laser propagation [9] were examined. These were then followed by experiments using ZBL at SNL where measurements of laser energy deposition [10] and energy losses due to stimulated Brillouin scattering (SBS) [11] were made. Significant progress has been made in the development of the MagLIF preheat platform. However, little has been done to assess the effect of an external magnetic field on the spatial distribution of plasma conditions.

Recently, analysis of spatially resolved spectra from Z experiments was used to extract electron temperature distributions $T_e(z)$ that were resolved only along the direction of laser propagation [12]. However, these axially resolved temperatures represent a spatial distribution of emissivity-weighted averages integrated over plasma regions along the instrument's line of sight. Thus, the challenge remained of measuring the spatial distribution $T_e(r, z)$ in order to make a detailed comparison with MHD simulations. Such measurements would provide an unprecedented characterization of laser heating in MagLIF cylindrical plasmas and enable a comparison with MHD simulations that would set a stringent test on the physics model employed in the simulations. Here we address this challenge by extracting $T_e(r, z)$ from the simultaneous and self-consistent analysis of a spatially resolved x-ray spectrum and a narrow-band x-ray image via multiobjective data analysis.

Multiobjective data analysis has been successfully used in the case of spherical implosion cores produced in ICF experiments performed at GEKKO XII and OMEGA, where it has been implemented to extract spatial distributions of

*kcarpenter2@unr.edu

electron temperature, density, and mix [13–19]. These applications were based on forward reconstruction, i.e., a physics model that took a spatial distribution of plasma conditions as input and produced synthetic approximations to multiple observations was used. The model was coupled to a Pareto genetic algorithm (PGA) [20,21] which performed the search in parameter space for the distribution(s) that produce the best simultaneous and self-consistent approximations to all pieces of data.

In this paper, we apply two separate multiobjective analysis methods to extract the electron temperature distribution $T_e(r, z)$ from spatially resolved spectra and narrow-band image data collected during MagLIF laser heating experiments. The first method utilizes a PGA that performs a two-objective optimization to determine electron temperature distributions that produce the best simultaneous and self-consistent approximations to a spatially resolved spectrum and narrow-band image intensity profile. Since the Ar line emission used in the analysis has small optical depth, a second method is performed in the optically thin approximation that solves a collection of constrained emissivity equations to extract the distribution of electron temperature. The application of two different methods that produce consistent results gives confidence in the extracted $T_e(r, z)$. With $T_e(r, z)$ measured in experiments with and without an external magnetic field, we examine how changes in thermal conduction due to the magnetic field change the values of T_e and the T_e spatial gradients. We also compare the experimental results with simulations and discuss the differences as well as tests that can be done to find the physics models and experimental parameters that will improve the agreement between simulations and experiments.

The layout of the paper is as follows. Section II presents the experiments and data collected. Section III discusses MHD simulations of the experiments and the postprocessing used to create synthetic data. Section IV describes the properties of the data and the two different methods used to extract $T_e(r, z)$. In Sec. V results from the analysis of synthetic data are shown to test the validity of the analysis methods. Next, the results from the experiments and simulations are shown in Sec. VI, where the effect of the magnetic field on the spatial temperature distribution and the temperature gradients is explored. Finally, a summary and conclusions are given in Sec. VII.

II. EXPERIMENTS AND DATA

The experiments were performed at Z [12]. The target was an 11.5-mm-tall Be liner with a 4.6 mm inner diameter and 0.1-mm-thick walls. There was a 3 mm diameter LEH at the top of the liner that was covered with a $1.77 \mu\text{m}$ polyimide foil. The liner was filled with 0.7 mg/cc of deuterium that was doped with a 0.1% atomic fraction of Ar. The Ar tracer was included to allow for spectroscopic diagnosis of the plasma. A schematic of the target is shown in Fig. 1.

The 527 nm ZBL [4] beam used to heat the D-Ar was smoothed with a distributed phase plate and had a circular 1.1 mm diameter focal spot. The laser pulse consisted of a prepulse and main pulse. The purpose of the 80 J, 0.5 ns prepulse was to heat and disassemble the LEH window prior

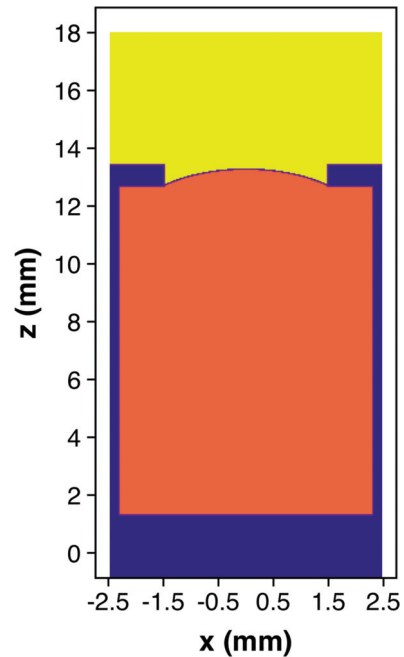


FIG. 1. A representative schematic of the target used in simulations. The blue region at the outer boundaries is the Be liner, the orange is the D-Ar gas fill, and the thin curved line at the top is the polyimide foil that covers the LEH. The laser beam propagates from top to bottom (i.e., in the $-z$ direction).

to the arrival of the main pulse. The main pulse reached the target 3.5 ns after the prepulse and delivered 1500 J in 3.2 ns.

Both experiments, H50 and H51, were nominally identical to each other in target geometry, filling conditions, and laser pulse. The difference between them was a magnetic field B_z oriented along the z axis of the liner. In H50, a pulsed coil magnet system [22] created a $B_z = 8.5$ T, while H51 was unmagnetized, i.e., $B_z = 0$ T. Since these experiments focused on the laser heating portion of MagLIF, the liners were not imploded.

A spherically bent Ge crystal spectrometer [23] was fielded and produced a time-integrated, axially resolved spectrum for each experiment. The spatial resolution of the instrument is $200 \mu\text{m}$, and the spectral resolving power is ~ 1900 . The spectra contain line emission in the 3100 eV to 3145 eV range from the $1s2p^1P_1 - 1s^2^1S_0$ He α resonance line w and the $1s2p^3P_1 - 1s^2^1S_0$ intercombination line y in He-like Ar as well as associated $n = 2-1$ satellite transitions in Li-like Ar [24].

In addition to the spectrometer, a spherically bent Ge crystal imaging diagnostic recorded time-integrated narrow-band images of the Ar emission in both experiments. The bandwidth is 7.5 eV and centered on the line y at 3124 eV. The images have axial and transverse spatial resolutions of $80 \mu\text{m}$ and $20 \mu\text{m}$, respectively.

The narrow-band images from both experiments are shown in Figs. 2(a) and 2(b), respectively. The images are on a linear scale and normalized to the maximum intensity recorded in the magnetized experiment. The direction of laser propagation is from top to bottom. The dashed lines in Fig. 2 represent the locations of the top and bottom boundaries of the liner's inner surface. A comparison of the two images shows that including

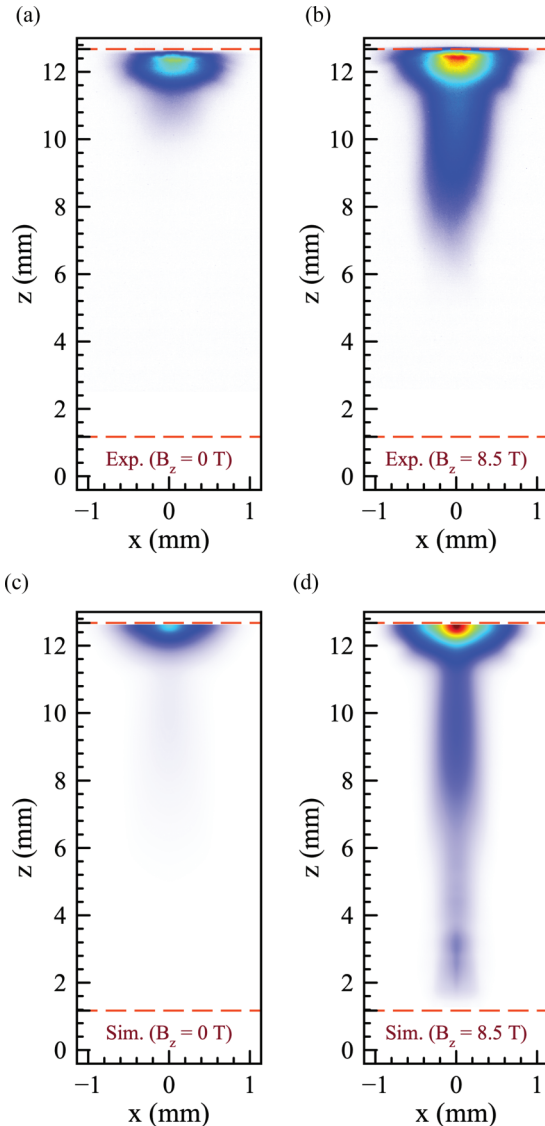


FIG. 2. Time-integrated narrow-band images from the experiments with (a) $B_z = 0$ T and (b) $B_z = 8.5$ T. Synthetic narrow-band images produced by postprocessing magneto-hydrodynamics simulations of the experiments with (c) $B_z = 0$ T and (d) $B_z = 8.5$ T. All images are on a linear color scale. The images in (a) and (b) are normalized to the maximum intensity in the magnetized experiment, and those in (c) and (d) are normalized to the maximum intensity from the simulation with an applied magnetic field.

the magnetic field results in an increase in both the amount of emission and axial extent of the emitting plasma. In the unmagnetized experiment, the emission decreases faster with increasing depth within the liner compared to the magnetized case.

III. MAGNETO-HYDRODYNAMICS SIMULATIONS

The radiation magnetohydrodynamics code HYDRA [25,26] was used to simulate both experiments. The simulations were performed using two-dimensional (2D) axisymmetric cylindrical geometry and utilized arbitrary Lagrangian-Eulerian mesh control. The MHD model was similar to the

one described in Ref. [27] and included self-generated magnetic fields due to the Biermann battery term and magnetic field advection due to the Nernst effect.

HYDRA modeled the entire experiment and included the D-Ar, polyimide foil, and Be liner as materials. Tabulated equations of state and an in-line NLTE model for the opacity were used. Radiation transport was implemented with an implicit Monte Carlo method. For the laser heating, HYDRA included inverse bremsstrahlung absorption, ray-tracing, and ponderomotive effects. Laser-plasma interactions such as SBS and stimulated Raman scattering (SRS) were not taken into account.

The resistivity and conductivity values were determined from tabular QMLD [28–30] models. Anisotropic thermal conduction due to the magnetic field was accounted for using the model of Epperlein-Haines [31]. The thermal conduction was flux limited with a flux-limiter value of 0.1 [9]. The Righi-Leduc term, which transports heat in the direction perpendicular to both the magnetic field and temperature gradient, was not included due to the azimuthal symmetry of the simulations.

The simulations were performed on a grid that had average axial and radial spatial resolutions of $38 \mu\text{m}$ and $18 \mu\text{m}$, respectively. For postprocessing, the HYDRA output was remapped onto a coarser grid that had a $200 \mu\text{m}$ axial resolution and $20 \mu\text{m}$ radial resolution. These values correspond to the axial and radial resolution of the spectrometer and imaging diagnostic, respectively.

The remapped time-history conditions were postprocessed using Spect3D [32], which produced synthetic time-integrated spectra and narrow-band images. The synthetic data presented in this paper were produced using time-dependent atomic kinetics with an escape factor to account for radiation transport effects in the level populations. An escape factor was used to make the postprocessing on a highly resolved grid computationally tractable. The postprocessing has been previously performed on coarser grids with nonlocal radiation transport which revealed that radiation transport effects only impact the resonance line w , a line we do not use in our analysis (see Sec. IV). The impact of transient atomic kinetics and radiation transport on the spectrum has also been investigated and is discussed in Ref. [12].

The synthetic images for the unmagnetized and magnetized cases are shown in Figs. 2(c) and 2(d), respectively. Each image is normalized to the maximum intensity of the simulation with an external magnetic field. Consistent with the experimental results, the image from the magnetized simulation contains emission from regions deeper within the liner than the unmagnetized case. However, in both cases the simulations overpredict the axial extent of the emission. The emission in the experimental images also extends farther in the radial direction than in the synthetic images. This is most noticeable in the magnetized case.

IV. ANALYSIS

A. Properties of the data

Shown in Fig. 3 is a plot of the emissivity of y , as predicted by the atomic kinetics code PrismSpect [33], integrated over

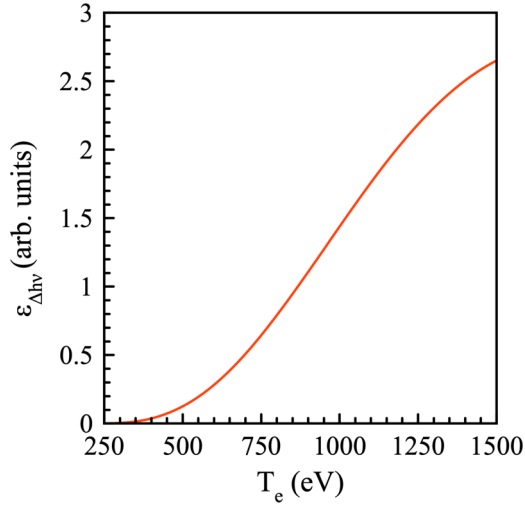


FIG. 3. Theoretical narrow-band emissivity $\varepsilon_{\Delta hv}$ as a function of T_e for $n_i = 2 \times 10^{20} \text{ cm}^{-3}$, and for a plasma that is 99.9% D and 0.1% Ar by atomic fraction. The bandwidth is 7.5 eV and centered on the line y at 3124 eV.

the photon energy range of the narrow-band images. The figure shows the emissivity as a function of T_e for a plasma that is 99.9% D and 0.1% Ar by atomic fraction and has an ion density $n_i = 2 \times 10^{20} \text{ cm}^{-3}$. These values are consistent with the initial conditions of the experiments. Like the spectrum, the narrow-band image shows sensitivity to T_e : as the temperature increases, so too does the emissivity.

An example of a spatially resolved spectrum with letter-labeled Li-like satellite transitions [24] is shown in Fig. 4(a). The intensities of the He-like Ar emission lines relative to the Li-like satellites can be used to extract electron temperature T_e [34]. For the conditions of the experiment, the relative satellite intensity distribution does not show sensitivity to electron density n_e [35]. In our work, we use the photon energy ranges 3100–3110 eV and 3120–3130 eV that contain the satellites j and k and the line y . Unlike the other transitions, these lines show negligible sensitivity to transient atomic kinetics and radiation transport effects [12].

We use line outs to produce a spatially resolved spectrum and a corresponding image intensity profile at each axial

location. An example pair from the magnetized experiment at $z = 8.8 \text{ mm}$ is shown in Fig. 4. In the following subsections, we describe two separate multiobjective analysis techniques that include both the spatially resolved spectra and narrow-band image intensity profiles to produce $T_e(r, z, B_z)$, where B_z is used to differentiate between the magnetized and unmagnetized cases. Due to the lack of density sensitivity in the relative intensity distributions of the spectra, the analysis is performed assuming a constant, uniform electron density $n_e = 2 \times 10^{20} \text{ cm}^{-3}$.

The analysis of axially resolved spectra results in T_e that are axially resolved but integrated over the radial coordinate r , i.e., $T_e(z)$. However, it is the simultaneous and self-consistent analysis of axially resolved spectra *and* axially and radially resolved narrow-band image intensity that holds the key for extracting the axially and radially resolved $T_e(r, z)$.

B. Pareto genetic algorithm search and reconstruction

The first analysis technique is a forward reconstruction method driven by a PGA. At each axial location z , the plasma is discretized into a disk that consists of a collection of rings that are functions of the radial coordinate r , each with a uniquely assigned $T_e(r, z)$. The outer radius of each disk is determined from the image size, and the thickness of each ring must be compatible with the measurement's spatial resolution. For any given temperature distribution $T_e(r, z)$, a physics model is used to transport radiation along chords, across the disk to produce a synthetic spectrum and a narrow-band image intensity distribution. The radiation transport is performed using a pretabulated database of temperature and photon-energy-dependent NLTE emissivity and opacity values calculated with PrismSpect.

The radiation transport model is coupled to a PGA [20,21] that drives a two-objective search in parameter space. For each z coordinate, the PGA searches for a radial temperature distribution $T_e(r, z)$ that produces the best simultaneous and self-consistent approximations to an axially resolved spectrum and narrow-band image radial intensity profile. The initial population of trial solutions is randomly generated and, thus, unbiased. After each iteration, the PGA updates the population based on the application of the genetic operators and Pareto domination and iterates until it converges to the collection of solutions that best approximate both pieces of data. No assumptions or restrictions are imposed on the shape of the temperature profiles, e.g. decreasing or increasing T_e with r . The PGA selects $T_e(r, z)$ based solely on how well the synthetic and experimental data agree. By changing the seed to the random number generator that initializes the algorithm, we can test the uniqueness of the solution(s) and also determine whether the best approximations to the data are defined by multiple local minima or one global minimum.

The PGA is good at identifying solutions near a minimum but is inefficient at producing refined solutions [15]. For this reason, we take the output solutions from the PGA and use them as initial seeds in a Levenberg-Marquardt, nonlinear least-squares routine [36,37] that produces the final $T_e(r, z)$. Schematics of the algorithm and radiation transport are shown in Figs. 5(a) and 5(b), respectively. Examples of the approximations to the experimental spectrum and image data, along

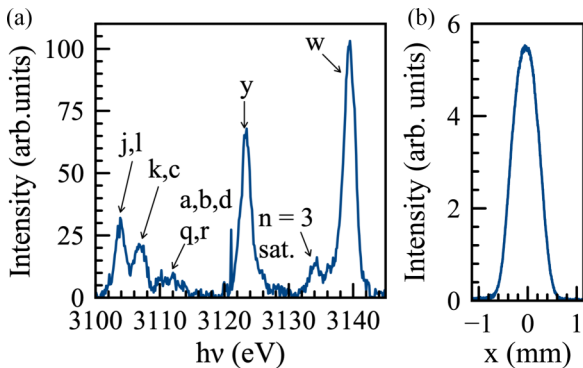


FIG. 4. Characteristic (a) Spatially resolved spectrum and (b) narrow-band image intensity profile produced from the magnetized experiment at $z = 8.8 \text{ mm}$.

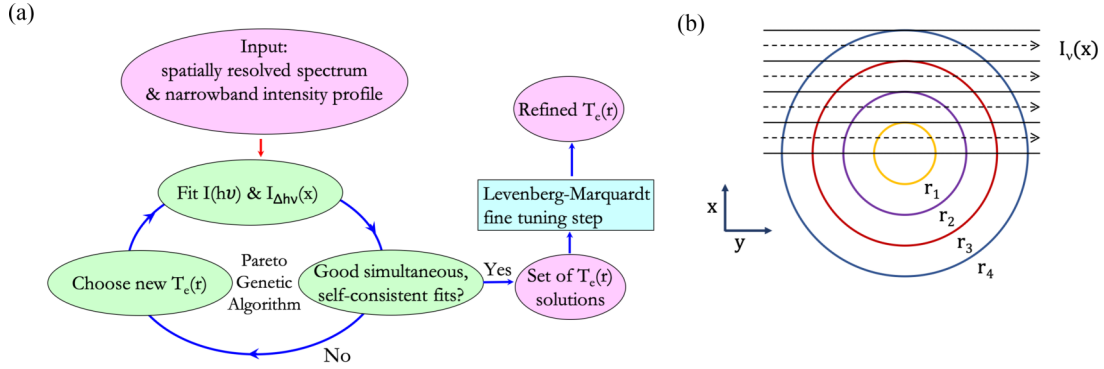


FIG. 5. (a) Schematic of the algorithm used in the multiobjective analysis based on forward reconstruction and driven by a PGA. (b) Example of the discretization of the plasma used at each z coordinate.

with the $T_e(r, z)$ solution, are shown in Fig 6. The examples are from the magnetized experiment at $z = 9.7$ mm. The synthetic spectrum in Fig. 6(a) is shown only for the photon energy ranges included in the analysis.

C. Quasianalytic emissivity analysis

An alternative to the forward reconstruction method is an emissivity analysis, performed under the optically thin approximation, that we call the quasianalytic method. In the optically thin limit, an Abel inversion of the narrow-band image will recover a radial emissivity distribution within the plasma. While no lines are truly optically thin, the optical depth τ of y is estimated to be less than 0.3, so we find the optically thin approximation to be reasonable. With the

Abel inverted images, we can solve a collection of emissivity equations to extract $T_e(r, z)$.

Just as in the forward reconstruction method, the analysis is performed one z coordinate at a time. Utilizing the T_e sensitivity of the narrow-band emissivity (see Fig. 3), we use the Abel inverted emissivity distributions to extract radially resolved temperature profiles $T_e(r, z)$. Since the images are not absolutely calibrated, a scaling constant k is needed to convert the experimental emissivity profiles from arbitrary to absolute units. The value of k is not known *a priori* but is solved for by constraining the emissivity-weighted average temperature of the disk $\langle T_e(z) \rangle$ [38] with the $\bar{T}_e(z)$ determined from the analysis of the corresponding axially resolved spectrum, i.e., $\langle T_e(z) \rangle = \bar{T}_e(z)$, with $\langle T_e(z) \rangle$ defined as

$$\langle T_e(z) \rangle = \frac{\int T_e(r, z) \varepsilon_{\Delta hv}^{th}(r, z) 2\pi r dr}{\int \varepsilon_{\Delta hv}^{th}(r, z) 2\pi r dr}, \quad (1)$$

where $\varepsilon_{\Delta hv}^{th}$ is the narrow-band emissivity.

Initially, a trial temperature $T_e(r = 0, z)$ is chosen, and the corresponding emissivity is determined. The value of k is then found by solving for $r = 0$:

$$\varepsilon_{\Delta hv}^{th} = k \varepsilon_{\Delta hv}^{exp}, \quad (2)$$

where $\varepsilon_{\Delta hv}^{exp}$ is the experimental emissivity in arbitrary units. Using the value of k , the rest of $\varepsilon_{\Delta hv}^{th}(r)$ are determined and used to solve for $T_e(r, z)$. The emissivity and temperature profiles are used to calculate $\langle T_e(z) \rangle$, which is compared to $\bar{T}_e(z)$. The scaling constant is updated, and the process is repeated until convergence is reached in $T_e(r, z)$ and the maximum fractional difference between the $\bar{T}_e(z)$ and $\langle T_e(z) \rangle$ values is within a chosen tolerance level. In this work a tolerance of 10^{-4} was used.

The plots in Figs. 7(a) and 7(b) show $T_e(r, z)$ from the experiments with ($B_z = 8.5$ T) and without ($B_z = 0$ T) an external magnetic field, respectively. The profiles from both methods show agreement. The consistency between the solutions, which were determined with two independent methods applied to same data set, confirms the uniqueness of the solution.

The error bars in the $T_e(r, z)$ profiles of Fig. 7 are the estimated uncertainties due to the noise in the data. In the PGA analysis, the uncertainties are determined from the covariance matrix that is calculated during the nonlinear least-squares

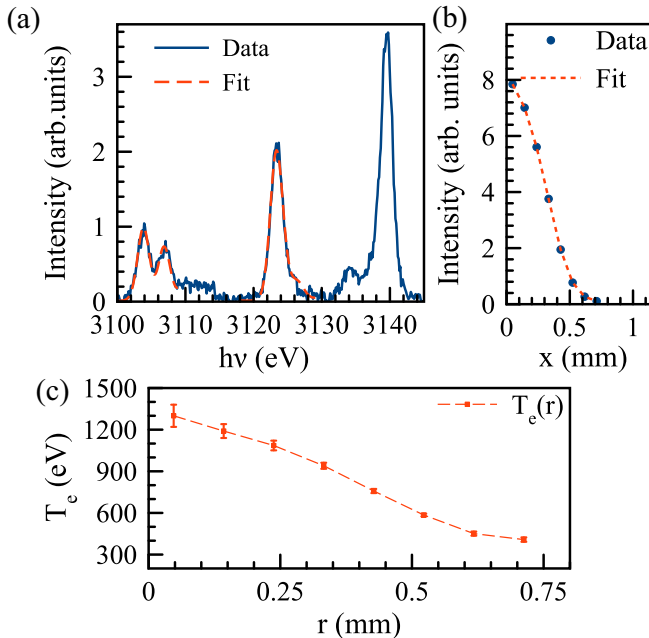


FIG. 6. Example of PGA analysis from the $B_z = 8.5$ T case at $z = 9.7$ mm. (a) Spatially resolved spectrum. (b) Narrow-band intensity profile. (c) Extracted electron temperature profile $T_e(r, z = 9.7$ mm, $B_z = 8.5$ T).

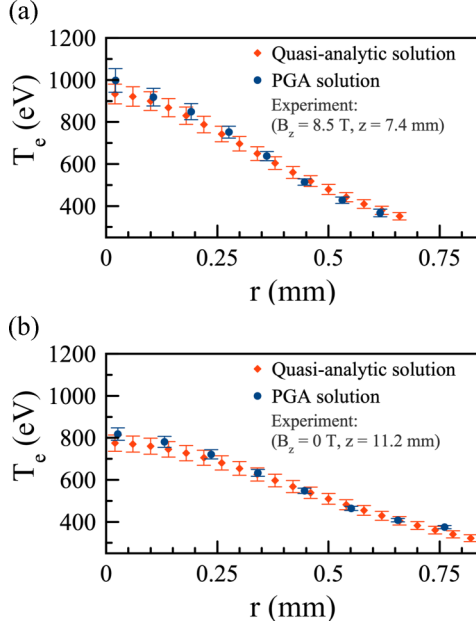


FIG. 7. Comparison of the $T_e(r, z)$ profiles extracted with the PGA (blue circles) and quasianalytic methods (orange diamonds) for (a) $B_z = 8.5$ T at $z = 7.4$ mm and (b) $B_z = 0$ T at $z = 11.2$ mm.

fine-tuning step [36]. For the quasianalytic method, the uncertainties in the image intensities are propagated through the Abel inversion to obtain emissivity uncertainties. The final uncertainty in each $T_e(r, z)$ value is dependent on the experimental emissivity uncertainty and the uncertainty in the $\overline{T_e}(z)$ from the analysis of the spectrum that is used to constrain the result. Another source of uncertainty is the choice of NLTE atomic kinetics code used for the analysis. A comparison of results from PrismSpect and SCRAM [39] in the analysis of the axially resolved spectra showed that SCRAM gives $\overline{T_e}(z)$ values that are ~ 100 eV lower than the PrismSpect results with similar spatial profiles [12].

V. TESTING ANALYSIS ON SYNTHETIC DATA

Since a constant uniform density was assumed in the analysis, it was important to assess how much density variations can affect the results. To this end, we used the synthetic data produced by postprocessing the simulations and analyzed it in the same way as the experimental data. The extracted $T_e^{sim}(r, z, B_z)$ were then compared to the emissivity-weighted averages $\langle T_e^{sim}(r, z, B_z) \rangle$ that were calculated using the time histories of the simulations. $\langle T_e^{sim}(r, z, B_z) \rangle$ is defined as

$$\langle T_e^{sim}(r, z, B_z) \rangle = \frac{\int T_e(r, z, t, B_z) \varepsilon_{hv}^y(r, z, t, B_z) dt}{\int \varepsilon_{hv}^y(r, z, t, B_z) dt}. \quad (3)$$

In Eq. (3), $T_e(r, z, t, B_z)$ is the HYDRA simulated electron temperature at time t and coordinates r and z , and $\varepsilon_{hv}^y(r, z, t)$ is the emissivity of y at the same position and time. The emissivity is determined from the atomic level populations calculated during postprocessing with Spect3D, and the integral in Eq. (3) is calculated over the entire time duration of the simulations.

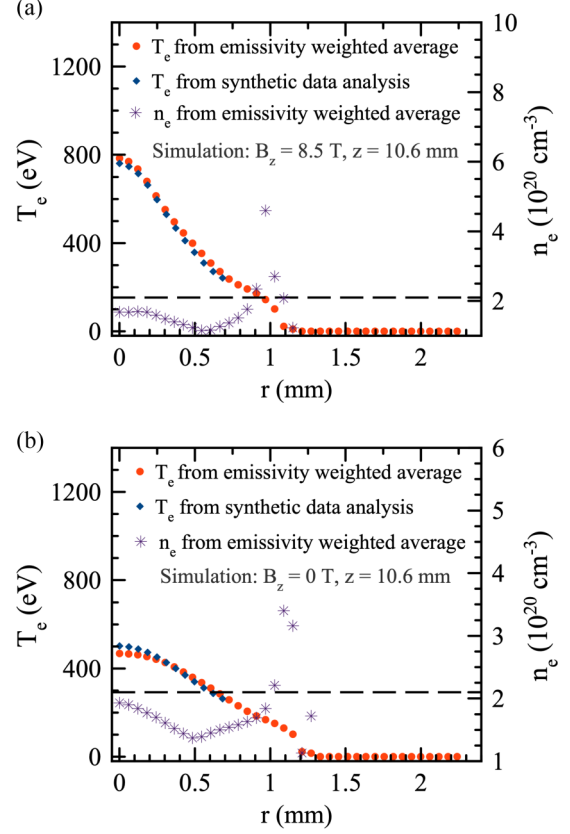


FIG. 8. Electron temperature and density profiles from the simulations at $z = 10.6$ mm with (a) $B_z = 8.5$ T and (b) $B_z = 0$ T. The orange circles are the emissivity-weighted average electron temperatures $\langle T_e^{sim}(r, z, B_z) \rangle$, the purple stars are the emissivity-weighted average electron density values $\langle n_e^{sim}(r, z, B_z) \rangle$, and the blue diamonds are the electron temperatures $T_e^{sim}(r, z, B_z)$ extracted through the analysis of the simulated data. The dotted black line represents the constant, uniform $n_e = 2 \times 10^{20} \text{ cm}^{-3}$ that is assumed in the analysis.

Similarly, we also calculated the emissivity-weighted average electron density $\langle n_e^{sim}(r, z, B_z) \rangle$, which is given by

$$\langle n_e^{sim}(r, z, B_z) \rangle = \frac{\int n_e(r, z, t, B_z) \varepsilon_{hv}^y(r, z, t, B_z) dt}{\int \varepsilon_{hv}^y(r, z, t, B_z) dt}. \quad (4)$$

In Eq. (4), $n_e(r, z, t, B_z)$ is the simulated time and space dependent electron density. These values are determined during the postprocessing using the temperature, mass density, and plasma composition information from the HYDRA simulations. With these values, the average ionization, and thus, the electron density within the plasma is determined by solving the sets of atomic rate equations.

For most of the z coordinates, the extracted $T_e^{sim}(r, z, B_z)$ compare well with the $\langle T_e^{sim}(r, z, B_z) \rangle$. Examples of $T_e^{sim}(r, z = 10.6 \text{ mm}, B_z)$ from the simulations with and without an external magnetic field are displayed in Fig. 8. The differences between the two profiles are within 10% in each case, and the largest differences occur at the center.

The $\langle n_e^{sim}(r, z, B_z) \rangle$ profiles demonstrate that fluid motion from the laser heating results in nonuniform density profiles. However, the extracted $T_e^{sim}(r, z, B_z)$ from the synthetic data

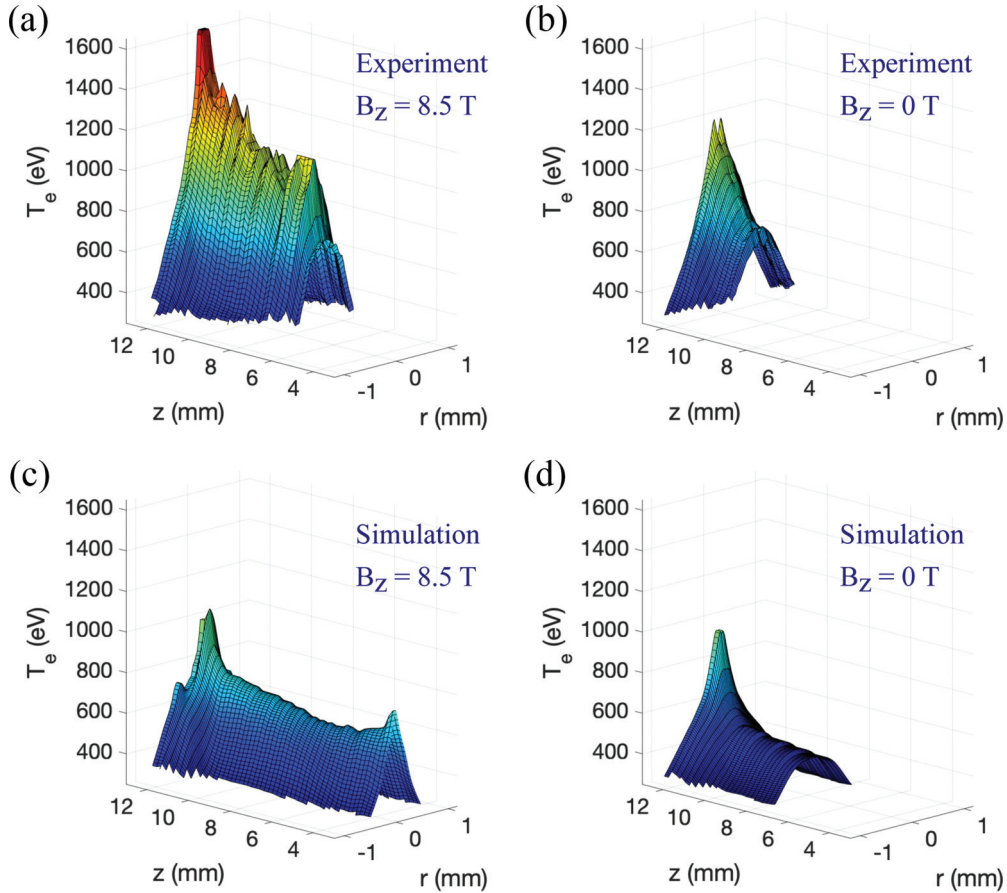


FIG. 9. Surface plots of the 2D temperature distributions $T_e(r, z, B_z)$ extracted by analyzing the experimental data and the synthetic data produced by postprocessing the simulations. (a) Experiment with a magnetic field ($B_z = 8.5$ T). (b) Experiment without a magnetic field ($B_z = 0$ T). (c) Simulation with a magnetic field ($B_z = 8.5$ T). (d) Simulation without a magnetic field ($B_z = 0$ T). The negative values of r are a result of reflecting the extracted temperature distributions about the axis of symmetry (z axis).

analysis compare well with $\langle T_e^{sim}(r, z, B_z) \rangle$. This suggests that assuming a constant uniform density in the analysis is reasonable. Furthermore, we have found that the sensitivity of the results to the assumed density is small. By assuming either $n_e = 1 \times 10^{20} \text{ cm}^{-3}$ or $n_e = 4 \times 10^{20} \text{ cm}^{-3}$, the average change in the extracted $T_e(r, z)$ values was less than 1%.

Other than fluid motion due to the laser heating, variations in n_e can also occur due to the mixing of window material with the D-Ar in regions near the LEH. The simulations suggest that, in the regions ~ 0.5 mm below the LEH, an increase in n_e up to five times the filling density can occur. Under those conditions the maximum differences between $T_e^{sim}(r, z, B_z)$ and $\langle T_e^{sim}(r, z, B_z) \rangle$ can reach 20%.

VI. RESULTS AND DISCUSSION

The extracted temperature profiles for each axial location were combined to form spatial temperature distributions resolved in both the radial and axial directions. In addition to the experimental data, we also analyzed the synthetic data produced by postprocessing the simulations. By doing so, we can assess how the experimental results compare to the simulation predictions. We designate the analysis results from the experimental and simulated synthetic data as $T_e^{exp}(r, z, B_z)$ and $T_e^{sim}(r, z, B_z)$, respectively.

Surface plots of the $T_e(r, z, B_z)$ are given in Fig. 9. Figures 9(a) and 9(b) are the results from the experiments, and Figs. 9(c) and 9(d) are from the analysis of the synthetic data from the postprocessing of the the simulations. In the experiments and the simulations, inclusion of an external magnetic field resulted in higher T_e values and increased the axial extent of the diagnosed plasma. Furthermore, in both cases, the simulations underpredicted T_e and overpredicted the axial extent of the laser-heated plasma.

Figure 10 shows examples of the $T_e(r, z, B_z)$ radial profiles for the experiments and simulations at different axial locations for both the magnetized and unmagnetized cases. Figure 10(a) is for $z = 11.4$ mm and Fig. 10(b) for $z = 10.4$ mm. With the magnetic field, radial thermal conduction is inhibited which results in higher values of T_e . The temperature differences between the magnetized and unmagnetized cases is maximum on axis and decreases with increasing radius. In both cases, the values of T_e from the simulations are lower than the experimental results, and the differences are largest for small radii. The differences are particularly large for the magnetized case where the experiment reaches a factor of $\sim 2\times$ hotter than the simulations predict.

We note that our Ar K-shell emission analysis can diagnose only regions where $T_e > 250$ eV. Thus, we are able to diagnose a volume of plasma in the magnetized case that

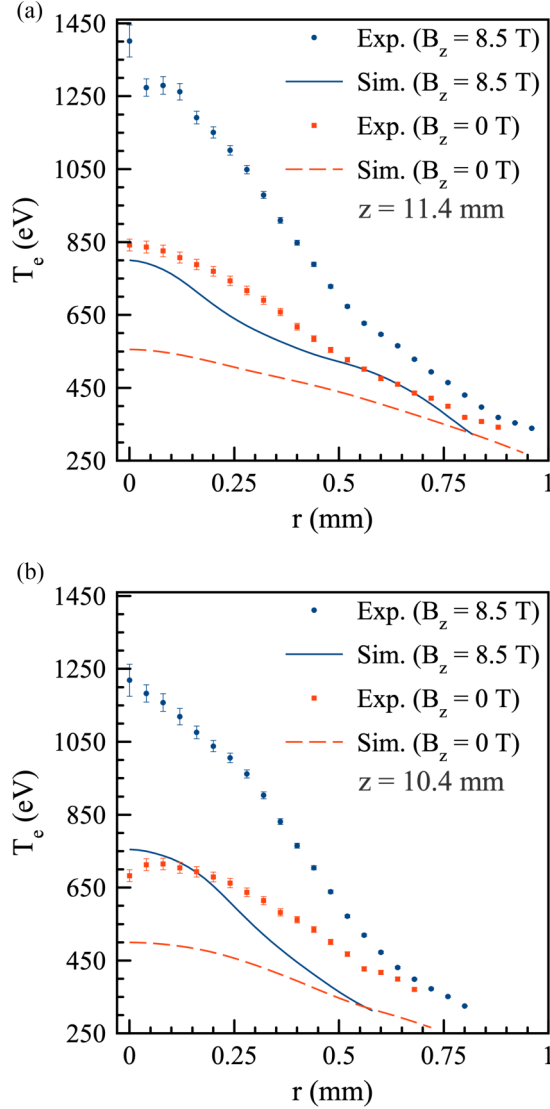


FIG. 10. Comparison of temperature profiles $T_e(r)$ between the magnetized ($B_z = 8.5$ T) and unmagnetized ($B_z = 0$ T) cases for the experiments and simulations at (a) $z = 11.4$ mm and (b) $z = 10.4$ mm.

is about a factor of two larger than in the unmagnetized case.

To further investigate the effect of the magnetic field, we took the extracted T_e values and evaluated the thermal conductivity based on the model of Epperlein-Haines [31]. According to the theory first developed by Braginskii [40], the thermal electron heat flux in the plasma can be written as

$$\mathbf{q}^e = -\chi_{\parallel}^e \nabla_{\parallel} T_e - \chi_{\perp}^e \nabla_{\perp} T_e, \quad (5)$$

where χ_{\parallel}^e and χ_{\perp}^e are the thermal conductivity values parallel and perpendicular to the magnetic field, respectively. When there is no magnetic field, the perpendicular conductivity is equal to the parallel component, which is the well-known Spitzer conductivity [41]. Based on the values of $T_e^{exp}(r, z, B_z = 8.5$ T), $\chi_{\perp}^e / \chi_{\parallel}^e$ ranges from 0.01 to 0.1, which indicates the electrons were highly magnetized.

We can also look at the temperature gradients within the plasma. In particular, we look at the gradients in the radial

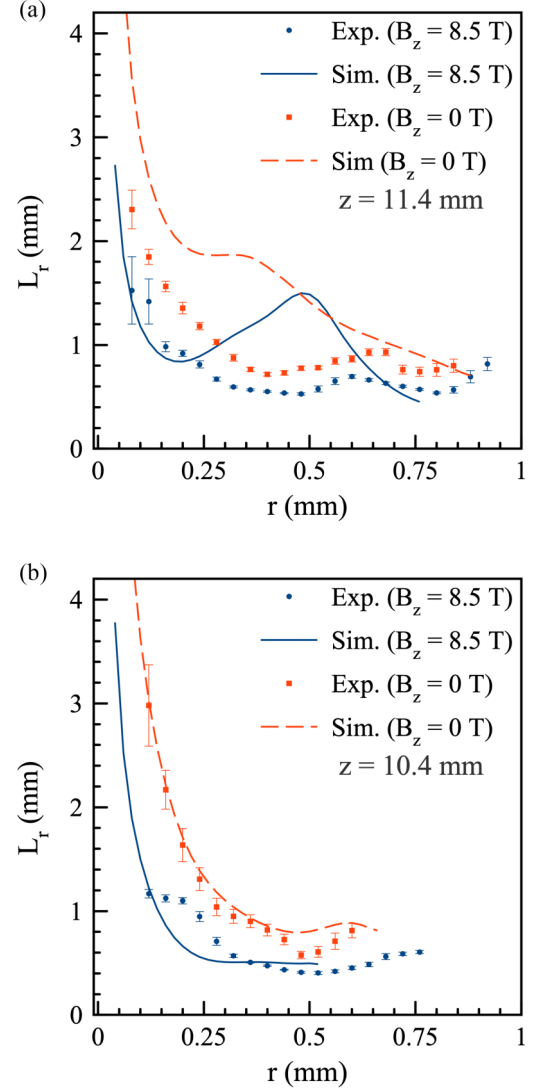


FIG. 11. Radial temperature gradient scale lengths, $L_r = T_e / |dT_e/dr|$ determined from the extracted temperature profiles for both the experiments and simulations at (a) $z = 11.4$ mm and (b) $z = 10.4$ mm.

direction, which is the direction where thermal conduction is inhibited. To assess the radial gradients, we use the gradient scale length $L_r = T_e / |dT_e/dr|$, where a shorter scale length indicates a larger gradient (or steeper temperature profile), and *vice versa*. For the calculation of the gradients, we performed a local linear fit to find the slope. At each radial point r , the fit was performed within a window that included the three neighboring points on each side of r . Figure 11 shows examples of the scale lengths for the same z locations as Fig. 10. The inhibited thermal conduction due to the magnetic field results in larger radial temperature gradients in the magnetized case compared to the unmagnetized case for both the experiments and simulations. Near the top of the liner, the experiments have steeper radial temperature profiles than in the simulations. Deeper within the liner, the radial gradients are comparable between the simulations and experiments.

The validity of local thermal transport is dependent on temperature gradient scale lengths that are large compared to the

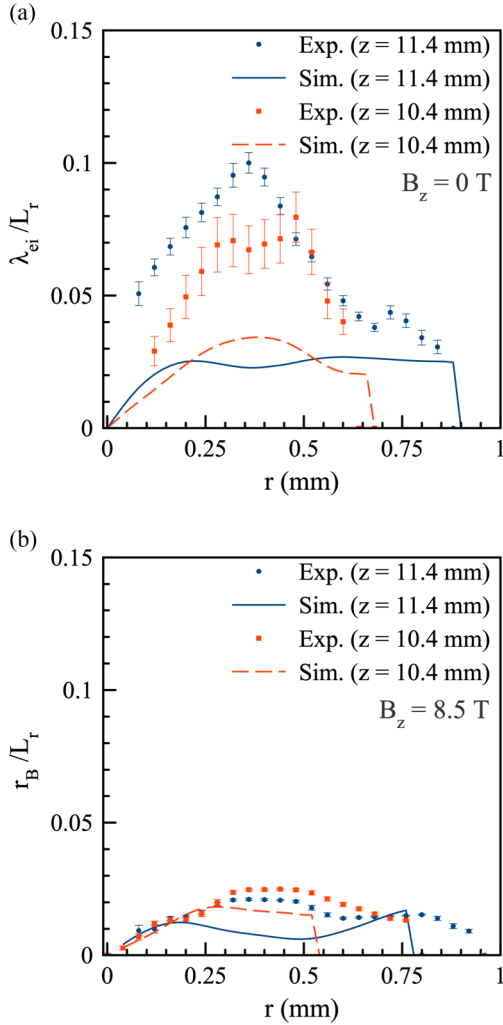


FIG. 12. (a) Ratios of the electron mean-free path λ_{ei} to the temperature gradient scale length L_r for the unmagnetized cases ($B_z = 0$ T). (b) Ratios of the electron gyro-radius r_B to L_r for the magnetized cases ($B_z = 8.5$ T).

electron-ion mean-free path $\lambda_{ei} = v_T \tau_{ei}$ [31,40]. The variables v_T and τ_{ei} are the electron thermal velocity and electron-ion collision time, respectively, and we use the equations that are given in Ref. [31]. Shown in Fig. 12(a) are plots of the electron mean-free path divided by the gradient scale length for the unmagnetized cases at $z = 11.4$ mm and 10.4 mm. Even for λ_{ei}/L_r as low as ~ 0.01 , local thermal transport can fail to give an accurate representation of the heat flux [31,42]. In both the simulations and experiments the ratios reach values that exceed 0.02. The ratios are larger in the experiments, where they can approach 0.1.

For magnetized plasmas, the threshold for the scale length is relaxed [31] and the effects of nonlocal thermal conduction can be reduced [43]. Since the magnetic field inhibits the radial electron motion, we compare the gradient scale length to the electron gyroradius, $r_B = m_e v_T / q_e B$ instead of λ_{ei} , where m_e is the mass of the electron, v_T is again the thermal electron velocity, q_e is the magnitude of the electron charge, and B is the magnetic field strength, which we assumed to be the value of the external axial magnetic field 8.5 T. For the

values of T_e in the experiments and simulations, r_B is less than λ_{ei} and the ratios r_B/L_r shown in Fig. 12(b) are smaller than the λ_{ei}/L_r in the unmagnetized cases. However, the ratios for the magnetized cases still exceed 0.01.

The large temperature gradients suggest that the experiments may have reached conditions where local thermal conduction models are no longer appropriate, especially in the unmagnetized case. It has been demonstrated previously that, when nonlocal effects are important, the experimental conditions in laser-heated plasmas can differ from those predicted by hydrodynamics simulations that use flux-limited local thermal conduction models [43–45]. Nonlocal effects can reduce the rate at which the laser propagates through the plasma and transport heat farther in the direction perpendicular to the beam than predicted by the flux-limited models [45]. This could help explain why the axial extent of the emission was shorter in the experiments than predicted by the simulations and why the experimental profiles of Fig. 10 extend farther radially than those from the simulations.

Another source of discrepancy could be thermal filamentation of the laser beam in the experiments that is not captured in the simulations [11]. Filamentation can effectively increase the radius of the laser beam and has been shown to reduce laser propagation through multimillimeter-scale plasmas [46]. This may be particularly important for the magnetized case where thermal filamentation is increased [47].

VII. SUMMARY AND CONCLUSIONS

Data analyses from two laser-heated plasma experiments related to the preheat stage in MagLIF have been discussed. In these experiments, 527 nm laser light from the Z-Beamlet laser was used to heat D contained within a cylindrical Be liner. The D was doped with a trace amount of Ar to allow for spectroscopy diagnosis. One of the experiments was unmagnetized, and the other included an 8.5 T axial magnetic field.

Argon K-shell line emission was observed, and, in each experiment, time-integrated spatially resolved spectra and a time-integrated narrow-band image were produced. The spectra have spatial resolution directed along the z axis of the liner and contain line emission from the He α resonance line w and intercombination line y in He-like Ar, as well as associated Li-like satellites. The image contains emission recorded over a 7.5 eV bandwidth centered on the line y at 3124 eV.

The spatially resolved spectra and narrow-band image data were included in two separate multiobjective analyses. In the first method, a physics model that produces synthetic data was coupled to a PGA. For each axial location z , the PGA performed a search in parameter space for the electron temperature distributions $T_e(r, z)$ that produced the best simultaneous and self-consistent approximations to both the spatially resolved spectra and narrow-band intensity profiles.

A second method was performed by making the optically thin approximation and Abel inverting the narrow-band images to obtain emissivity radial distributions within the plasma. At each z coordinate, a collection of emissivity equations was solved to extract $T_e(r, z)$. The emissivity-weighted average $\langle T_e(z) \rangle$ was constrained with $\overline{T_e(z)}$ obtained by the individual analysis of the spatially resolved spectra.

Each technique produced 2D electron temperature distributions $T_e(r, z, B_z)$, and the results were consistent between them. In both experiments, the plasma was hottest at $r = 0$ and near the top of the liner. In the magnetized case, the plasma reached higher T_e and extended deeper within the liner. The radial thermal conduction due to the magnetic field also resulted in larger radial temperature gradients than in the unmagnetized case.

Analysis of synthetic data from postprocessed simulations showed that the extracted values represent emissivity-weighted averaged values of temperature. The results from the analysis of the synthetic data were compared with those from experiments. This showed that the simulations underpredicted the temperature values in both cases. The differences are greatest near the central regions of the plasma, i.e., $r = 0$. The simulation and experiment differences are larger in the magnetized case where the simulated values are up to a factor of two lower than the experimental results.

Using the extracted temperature profiles, we calculated the radial temperature gradients. The scale lengths of the experimental temperature gradients compared to the electron mean-free path in the unmagnetized case and gyroradius in the magnetized were such that nonlocal thermal conduction effects may be important, particularly in the unmagnetized experiment. The magnitude of these effects could be tested with simulations using both traditional flux-limited thermal conduction and nonlocal thermal transport models. Furthermore, simulations that can more accurately model the laser beam would help demonstrate the effects of LPI such as filamentation, which could also be important in both cases.

Along with the tests described in the previous paragraph, our analysis could be performed on experiments that used different magnetic field strengths, laser intensities, laser beam smoothing, and LEH foil thicknesses. Performing simulation and experiment comparisons for multiple configurations would help unfold the regions of parameter space that can be accurately simulated with current models and when more complex physics such as nonlocal thermal conduction and laser-plasma interactions are needed. The PGA analysis is general and can be extended to include more measurements and could be applied to time-resolved data as well. The ability to extract the 2D resolved temperature distributions affords the opportunity to perform detailed comparisons with simulations that aren't possible with results from analysis that considers only one piece of data at a time.

ACKNOWLEDGMENTS

This work was supported by Contract No. 1575018 with SNL. SNL is a multi-mission laboratory managed and operated by the National Technology & Engineering Solutions of Sandia, LLC., a wholly owned subsidiary of Honeywell International, Inc., U.S. Department of Energy's National Nuclear Security Administration, under Contract No. DE-NA0003525. This paper describes objective technical results and analysis. Any subjective views or opinions that might be expressed in the paper do not necessarily represent the views of the U.S. Department of Energy or the United States Government.

-
- [1] S. A. Slutz, M. C. Herrmann, R. A. Vesey, A. B. Sefkow, D. B. Sinars, D. C. Rovang, K. J. Peterson, and M. E. Cuneo, *Phys. Plasmas* **17**, 056303 (2010).
 - [2] M. R. Gomez, S. A. Slutz, A. B. Sefkow, D. B. Sinars, K. D. Hahn, S. B. Hansen, E. C. Harding, P. F. Knapp, P. F. Schmit, C. A. Jennings *et al.*, *Phys. Rev. Lett.* **113**, 155003 (2014).
 - [3] S. B. Hansen, M. R. Gomez, A. B. Sefkow, S. A. Slutz, D. B. Sinars, K. D. Hahn, E. C. Harding, P. F. Knapp, P. F. Schmit, T. J. Awe *et al.*, *Phys. Plasmas* **22**, 056313 (2015).
 - [4] P. K. Rambo, I. C. Smith, J. L. Porter, M. J. Hurst, C. S. Speas, R. G. Adams, A. J. Garcia, E. Dawson, B. D. Thurston, C. Wakefield *et al.*, *Appl. Opt.* **44**, 2421 (2005).
 - [5] A. B. Sefkow, S. A. Slutz, J. M. Koning, M. M. Marinak, K. J. Peterson, D. B. Sinars, and R. A. Vesey, *Phys. Plasmas* **21**, 072711 (2014).
 - [6] S. A. Slutz, W. A. Stygar, M. R. Gomez, K. J. Peterson, A. B. Sefkow, D. B. Sinars, R. A. Vesey, E. M. Campbell, and R. Betti, *Phys. Plasmas* **23**, 022702 (2016).
 - [7] S. A. Slutz, M. R. Gomez, S. B. Hansen, E. C. Harding, B. T. Hutsel, P. F. Knapp, D. C. Lamppa, T. J. Awe, D. J. Ampleford, D. E. Bliss *et al.*, *Phys. Plasmas* **25**, 112706 (2018).
 - [8] A. J. Harvey-Thompson, A. B. Sefkow, T. N. Nagayama, M. S. Wei, E. M. Campbell, G. Fiksel, P.-Y. Chang, J. R. Davies, D. H. Barnak, V. Y. Glebov *et al.*, *Phys. Plasmas* **22**, 122708 (2015).
 - [9] A. J. Harvey-Thompson, A. B. Sefkow, M. S. Wei, T. Nagayama, E. M. Campbell, B. E. Blue, R. F. Heeter, J. M. Koning, K. J. Peterson, and A. Schmitt, *Phys. Rev. E* **94**, 051201(R) (2016).
 - [10] A. J. Harvey-Thompson, M. Geissel, C. A. Jennings, M. R. Weis, M. R. Gomez, J. R. Fein, D. J. Ampleford, G. A. Chandler, M. E. Glinsky, K. D. Hahn *et al.*, *Phys. Plasmas* **26**, 032707 (2019).
 - [11] M. Geissel, A. J. Harvey-Thompson, T. J. Awe, D. E. Bliss, M. E. Glinsky, M. R. Gomez, E. Harding, S. B. Hansen, C. Jennings, M. W. Kimmel *et al.*, *Phys. Plasmas* **25**, 022706 (2018).
 - [12] K. R. Carpenter, R. C. Mancini, E. C. Harding, A. J. Harvey-Thompson, M. Geissel, M. R. Weis, S. B. Hansen, K. J. Peterson, and G. A. Rochau, *Phys. Plasmas* **27**, 052704 (2020).
 - [13] I. Golovkin, R. Mancini, S. Louis, Y. Ochi, K. Fujita, H. Nishimura, H. Shirga, N. Miyanaga, H. Azechi, R. Butzbach *et al.*, *Phys. Rev. Lett.* **88**, 045002 (2002).
 - [14] L. A. Welser, R. C. Mancini, J. A. Koch, N. Izumi, S. J. Louis, I. E. Golovkin, T. W. Barbee, S. W. Haan, J. A. Delettrez, F. J. Marshall *et al.*, *J. Quant. Spectrosc. Radiat. Transfer* **99**, 649 (2006).
 - [15] T. Nagayama, R. C. Mancini, L. A. Welser, S. Louis, I. E. Golovkin, R. Tommasini, J. A. Koch, N. Izumi, J. Delettrez, F. J. Marshall *et al.*, *Rev. Sci. Instrum.* **77**, 10F525 (2006).
 - [16] L. Welser-Sherrill, R. C. Mancini, J. A. Koch, N. Izumi, R. Tommasini, S. W. Haan, D. A. Haynes, I. E. Golovkin, J. A. Delettrez, F. J. Marshall *et al.*, *High Energy Density Phys.* **3**, 287 (2007).

- [17] L. Welsler-Sherrill, R. C. Mancini, J. A. Koch, N. Izumi, R. Tommasini, S. W. Haan, D. A. Haynes, I. E. Golovkin, J. J. MacFarlane, J. A. Delettrez *et al.*, *Phys. Rev. E* **76**, 056403 (2007).
- [18] T. Nagayama, R. C. Mancini, R. Florido, R. Tommasini, J. A. Koch, J. A. Delettrez, S. P. Regan, V. A. Smalyuk, L. A. Welsler-Sherrill, and I. E. Golovkin, *Rev. Sci. Instrum.* **79**, 10E921 (2008).
- [19] T. Nagayama, R. C. Mancini, R. Florido, D. Mayes, R. Tommasini, J. A. Koch, J. A. Delettrez, S. P. Regan, and V. A. Smalyuk, *Phys. Plasmas* **19**, 082705 (2012).
- [20] D. E. Goldberg, *Genetic Algorithms in Search, Optimization, and Machine Learning* (Addison-Wesley, New York, 1989).
- [21] K. Deb, *Multi-objective Optimization Using Evolutionary Algorithms* (John Wiley & Sons, New York, 2009).
- [22] D. C. Rovang, D. C. Lamppa, M. E. Cuneo, A. C. Owen, J. McKenney, D. W. Johnson, S. Radovich, R. J. Kaye, R. D. McBride, C. S. Alexander *et al.*, *Rev. Sci. Instrum.* **85**, 124701 (2014).
- [23] E. C. Harding, T. Ao, J. E. Bailey, G. Loisel, D. B. Sinars, M. Geissel, G. A. Rochau, and I. C. Smith, *Rev. Sci. Instrum.* **86**, 043504 (2015).
- [24] A. H. Gabriel, *Mon. Not. R. Astron. Soc.* **160**, 99 (1972).
- [25] M. M. Marinak, S. W. Haan, T. R. Dittrich, R. E. Tipton, and G. B. Zimmerman, *Phys. Plasmas* **5**, 1125 (1998).
- [26] M. M. Marinak, G. D. Kerbel, N. A. Gentile, O. Jones, D. Munro, S. Pollaine, T. R. Dittrich, and S. W. Haan, *Phys. Plasmas* **8**, 2275 (2001).
- [27] W. A. Farmer, J. M. Koning, D. J. Strozzi, D. E. Hinkel, L. F. B. Hopkins, O. S. Jones, and M. D. Rosen, *Phys. Plasmas* **24**, 052703 (2017).
- [28] Y. T. Lee and R. M. More, *Phys. Fluids* **27**, 1273 (1984).
- [29] M. Desjarlais, *Contrib. Plasma Phys.* **41**, 267 (2001).
- [30] M. P. Desjarlais, J. D. Kress, and L. A. Collins, *Phys. Rev. E* **66**, 025401(R) (2002).
- [31] E. M. Epperlein and M. G. Haines, *Phys. Fluids* **29**, 1029 (1986).
- [32] J. J. MacFarlane, I. E. Golovkin, P. Wang, P. R. Woodruff, and N. A. Pereyra, *High Energy Density Phys.* **3**, 181 (2007).
- [33] J. J. MacFarlane, I. E. Golovkin, P. R. Woodruff, D. R. Welch, B. V. Oliver, T. A. Mehlhorn, and R. B. Campbell, in *Inertial Fusion Sciences and Applications 2003*, edited by B. A. Hammel, D. D. Meyerhofer, and J. J. Meyer-ter-Vehn (American Nuclear Society, 2004), p. 457.
- [34] A. H. Gabriel and T. M. Paget, *J. Phys. B: At. Mol. Phys.* **5**, 673 (1972).
- [35] V. L. Jacobs, J. E. Rogerson, M. H. Chen, and R. D. Cowan, *Phys. Rev. A* **32**, 3382 (1985).
- [36] W. H. Press, B. P. Flannery, S. A. Teukolsky, and W. T. Vetterling, *Numerical Recipes in C* (Cambridge University Press, Cambridge, 1997).
- [37] M. K. Transtrum and J. P. Sethna, [arXiv:1201.5885](https://arxiv.org/abs/1201.5885) [physics.data-an] (2012).
- [38] I. E. Golovkin and R. C. Mancini, *J. Quant. Spectrosc. Radiat. Transfer* **65**, 273 (2000).
- [39] S. B. Hansen, J. Bauche, C. Bauche-Arnoult, and M. F. Gu, *High Energy Density Phys.* **3**, 109 (2007).
- [40] S. I. Braginskii, *Reviews of Plasma Physics* (Consultants Bureau, New York, 1965), Vol I, pp. 205–311.
- [41] L. Spitzer and R. Härm, *Phys. Rev.* **89**, 977 (1953).
- [42] W. A. Farmer, O. S. Jones, M. A. Barrios, D. J. Strozzi, J. M. Koning, G. D. Kerbel, D. E. Hinkel, J. D. Moody, L. J. Suter, D. A. Liedahl *et al.*, *Plasma Phys. Control. Fusion* **60**, 044009 (2018).
- [43] D. H. Froula, J. S. Ross, B. B. Pollock, P. Davis, A. N. James, L. Divol, M. J. Edwards, A. A. Offenberger, D. Price, R. P. J. Town *et al.*, *Phys. Rev. Lett.* **98**, 135001 (2007).
- [44] G. Gregori, S. H. Glenzer, J. Knight, C. Niemann, D. Price, D. H. Froula, M. J. Edwards, R. P. J. Town, A. Brantov, W. Rozmus, and V. Y. Bychenkov, *Phys. Rev. Lett.* **92**, 205006 (2004).
- [45] N. B. Meezan, L. Divol, M. M. Marinak, G. D. Kerbel, L. J. Suter, R. M. Stevenson, G. E. Slark, and K. Oades, *Phys. Plasmas* **11**, 5573 (2004).
- [46] S. H. Glenzer, D. H. Froula, L. Divol, M. Dorr, R. L. Berger, S. Dixit, B. A. Hammel, C. Haynam, J. A. Hittinger, J. P. Holder *et al.*, *Nat. Phys.* **3**, 716 (2007).
- [47] H. C. Watkins and R. J. Kingham, *Phys. Plasmas* **25**, 092701 (2018).